ChemPubSoc Europe

DOI: 10.1002/cssc.201802500

CHEMSUSCHEM Full Papers

Atomic Layer Deposition of $NiOOH/Ni(OH)_2$ on PIM-1-Based N-Doped Carbon Nanofibers for Electrochemical Water Splitting in Alkaline Medium

Bhushan Patil,*[a] Bekir Satilmis,[a, b] Mohammad Aref Khalily,[a] and Tamer Uyar*[a, c]

Portable and flexible energy devices demand lightweight and highly efficient catalytic materials for use in energy devices. An efficient water splitting electrocatalyst is considered an ideal future energy source. Well-aligned high-surface-area electrospun polymers of intrinsic microporosity (PIM-1)-based nitrogen-doped carbon nanofibers were prepared as a free-standing flexible electrode. A non-noble-metal catalyst $NiOOH/Ni(OH)_2$ was precisely deposited over flexible free-standing carbon nanofibers by using atomic layer deposition (ALD). The morphology, high surface area, nitrogen doping, and Ni states synergistically showed a low onset potential ($\eta_{HER} = -40$ and $\eta_{OER} = 290$ mV vs. reversible hydrogen electrode), small overpotential at η_{10} [oxygen evolution reaction (OER) = 390.5 mV and hydrogen evolution reaction (HER) = −147 mV], excellent kinetics (Tafel slopes for OER = 50 mV dec^{-1} and HER = 41 mV dec^{-1}), and high stability (> 16 h) towards water splitting in an alkaline medium (0.1 M KOH). The performance was comparable with that of state-of-the-art noble-metal catalysts (e.g., Ir/C, Ru/C for OER, and Pt/C for HER). Post-catalytic characterization with X-ray photoelectron spectroscopy (XPS) and Raman spectroscopy further proved the durability of the electrode. This study provides insight into the design of 1D-aligned N-doped PIM-1 electrospun carbon nanofibers as a flexible and free-standing $NiOOH/Ni(OH)_2$ decorated electrode as a highly stable nanocatalyst for water splitting in an alkaline medium.

Introduction

The future of flexible energy devices demands pioneering breakthrough design of cheap, sustainable, and efficient systems for the conversion and storage of renewable energy. The production of hydrogen and oxygen through water splitting seems a promising solution through the hydrogen evolution reaction (HER) and the oxygen evolution reaction (OER) owing to its high energy conversion efficiency, negligible environment pollution, and potentially wide range of applications such as fuel cells and hydrogen production. The Pt-group metals and Ir/Ru-based compounds have been the benchmark state-of-the-art catalysts for the HER and OER, respectively.[1,2] Despite the better catalytic activity of these catalysts, their high cost, scarcity, and poor stability limit their commercial and widespread use. Therefore, enormous efforts have been devoted to replacing these catalysts with non-noble-metal-based, abundant, and highly efficient electrocatalysts for water splitting such as VSe_2,[3] Co oxide,[4,5] and Fe oxide.[6] The challenge of using such non-noble-metal catalysts for water splitting in an alkaline solution is their instability. Ni has a similar binding energy with hydrogen as Pt[7,8] and has been widely considered and applied as a water-splitting catalyst in various forms such as sea-urchin-shaped $Ni_3(VO_4)_2$,[9] bimetallic NiMoN nanowires,[10] and Ni_3Se_2.[11] Therefore, Ni and Ni oxides are promising non-noble-metal catalysts for the replacement of expensive noble-metal catalysts. Ni oxide has already been shown to be an efficient OER catalyst in alkaline media.[12,13] However, to the best of our knowledge, no studies have shown an effective catalytic activity of $NiOOH/Ni(OH)_2$-coated carbon nanofiber electrodes towards HER in alkaline media. Furthermore, an ideal catalyst must be efficient in the same pH range for both HER and OER. Therefore, we used $NiOOH/Ni(OH)_2$ as a facile catalyst for water splitting in alkaline media.

Electrospinning is a widely used technique for the synthesis of controlled dimensional free-standing nanofibers owing to its versatility and simplicity.[14] Electrospun free-standing carbon fibers have been used for several different applications including photocatalysis,[15,16] supercapacitors,[17] sensors,[18,19] and water filtration.[20,21] The polymer of intrinsic microporosity (PIM-1) has a high fractional free-volume (26%) and is reported to have a BET surface area of 760 m^2 g^{-1}. Therefore, among carbonized fibers, PIM-1-based ultrafine carbon nanofibers have a

[a] Dr. B. Patil, Dr. B. Satilmis, Dr. M. A. Khalily, Prof. Dr. T. Uyar
Institute of Materials Science and Nanotechnology
Bilkent University
Ankara, 06800 (Turkey)
E-mail: bhushanpatil25@gmail.com
uyar@unam.bilkent.edu.tr

[b] Dr. B. Satilmis
Faculty of Arts and Science, Department of Chemistry
Ahi Evran University
Kirsehir 40100 (Turkey)

[c] Prof. Dr. T. Uyar
Department of Fiber Science & Apparal Design, College of Human Ecology
Cornell University
Ithaca, New Yor 14853 (USA)
E-mail: tu46@cornell.edu

Supporting Information and the ORCID identification number(s) for the author(s) of this article can be found under: https://doi.org/10.1002/cssc.201802500.

high surface area with a microporous morphology, which are desired characteristics for the selection of an electrode material.[22] Furthermore, simple pyrolysis of such electrospun ultrafine PIM-1 fibers can produce nitrogen-doped carbon fibers.[20] Nitrogen-doped carbon fibers are more efficient than normal carbon fibers in water splitting.[23] In addition, nitrogen-doped carbon fibers act as an excellent stabilizer for metal nanoparticles.[24] Therefore, electrospun PIM-1-based aligned nitrogen-doped carbon nanofibers (PIM-CF) were chosen for the fabrication of free-standing flexible electrodes to deposit NiOOH/$Ni(OH)_2$ catalyst. Furthermore, binders used in electrocatalysts increase the resistance of the electrode and deplete the catalytic performance. Therefore, it is always preferable to avoid using a binder or to design binder-free electrodes.[25,26] From this perspective, N-doped PIM-CF provides a binder-free support for the NiOOH/$Ni(OH)_2$ catalyst.

Precise, uniform, and atomic-level deposition of metals and metal oxides by using atomic layer deposition (ALD) has become an attractive tool owing to its self-limiting nature.[27,28] The ALD process is based on the binary reaction in a sequential fashion with atomic-level control.[29] To grow the desired thickness of the material, these binary steps are repeated and the conditions reflect the deposition per ALD cycle.[30] It has been reported as a versatile technique for the functionalization of electrospun fibers with numerous metal oxides such as Pt,[31] Pd,[32] Zn,[33] and Ru.[24] In addition, controlling the facets[34] and operating at a lower temperature than a conventional chemical vapor deposition technique widens its application for numerous nanoparticles and thin-film deposition. Therefore, the ALD method was chosen to prepare a uniform thin coating of Ni oxyhydroxy catalysts on PIM-CF.

Herein, we report a simple and controlled synthesis of flexible, free-standing, binder-free, atomically deposited NiOOH/$Ni(OH)_2$ on well-aligned N-doped PIM-CF and its application towards overall water splitting (i.e., HER and OER) in an alkaline medium. The stability of these electrodes was measured by cyclic voltammetry (CV) and chronoamperometry (CA), and the structure of the material post-catalysis, specifically, the state of Ni and carbon, was characterized by X-ray photoelectron spectroscopy (XPS) and Raman spectroscopy. To the best of our knowledge, this is the first report of ALD of NiOOH/$Ni(OH)_2$ on free-standing flexible PIM-CF for OER and HER catalysis in an alkaline medium.

Results and Discussion

Electrospun PIM-1 fibers have a bright yellow color that completely changes and turns into carbon black after carbonization, as shown in Figure 1A. ALD of NiOOH/$Ni(OH)_2$ does not have any visible influence on the fiber morphology. The free-standing PIM-1 fibers exhibit significant bending stability, which is maintained after carbonization and ALD of the NiOOH/$Ni(OH)_2$ coating (Figure 1B,C). The SEM image of PIM-CF showed well-aligned carbon fibers with an average diameter of approximately 2 μm (Figure 1D and Figure S1 in the Supporting Information). The characterization of PIM-1 is now well-documented; it shows characteristic nitrile stretches in the Fourier-transform IR (FTIR) spectra.[35] An absence of the characteristic nitrile (2240 cm^{-1}) and ether stretches (1265 cm^{-1}) was observed for PIM-CF (Figure 1E), which indicated the successful carbonization of PIM to PIM-CF.[36] The powder X-ray diffraction (PXRD) pattern of PIM-CF (Figure S2 in the Supporting Information) displayed a typical characteristic (100) graphene plane associated with the 2.05 Å peak of PIM-CF.[37] It has been reported that pristine and partially carbonized PIM has a broad trimodal XRD pattern sintered into amorphous carbon configurations, which was absent in PIM-CF and further confirmed the complete carbonization of PIM-1.[37] From a molecular perspective, to characterize the molecular structure of the materials in a meaningful manner, it was necessary to measure the Raman spectrum. Raman peaks (Figure 1F) were deconvoluted in to D, G, D3, and D4 at 1315, 1590, 1522, and 1169 cm^{-1} representing disordered, graphitic, sp^2–sp^3 carbon bonds, and amorphous carbon, respectively.[17] The I_D/I_G ratio of the intensities of the D and G bands is the measure of crystallinity or degree of ordered carbon molecules, which was 1.68 for PIM-CF. The ratio was in close agreement with the reported value for carbonized PIM-1 ($I_D/I_G = 1.8$).[20]

XPS high-resolution spectra of carbon, nitrogen, and oxygen are shown in Figure 1G and H and Figure S3B in the Supporting Information, respectively. The C1s spectrum (Figure 1G) indicated that the largest peak at 284.8 eV was associated with graphitic carbon, whereas the peaks at 285.5, 286.0, and (288 ± 0.2) eV were assigned to C–OH/C–N, C=O/C–O–C, and C=O/C=N, respectively. The N1s spectrum (Figure 1H) clearly showed the presence of nitrogen doping in PIM-CF with pyridinic, pyrrolic, and graphitic nitrogen assigned to the peaks at 398.3, 400.0, and (401.1 ± 0.2) eV, respectively. The atomic contribution of carbon, oxygen, and nitrogen were 92.05, 4.99, and 2.96%, respectively. Although the oxygen content in PIM-CF was very low, the O1s spectrum (Figure S3B in the Supporting Information) was deconvoluted to understand the contribution from C–O, C=O, and chemisorbed water molecules at 530.0, 532.5, and (534.0 ± 0.2) eV, respectively.

The morphology of Ni@PIM-CF and the distribution of Ni on PIM-CF was analyzed by SEM (Figure 2A, and Figures S4 and S5 in the Supporting Information) and TEM (Figure S6 in the Supporting Information). The SEM images of PIM-CF (Figure 1D) and Ni@PIM-CF (Figure 2A) were analogous with each other, indicating negligible morphology changes after NiOOH/$Ni(OH)_2$ deposition and ozone treatment during ALD of PIM-CF. The uniform distribution of the NiOOH/$Ni(OH)_2$ on PIM-CF was confirmed by elemental mapping (Figure 2B), which indicated an atomic ratio of 81.14, 15.22, and 0.63 for C, O, and Ni, respectively. The elemental energy dispersive X-ray spectroscopy (EDS) line map confirmed the Ni-coating over PIM-CF, which was further confirmed by multipoint EDS (Figure S6 in the Supporting Information). The FTIR spectrum of Ni@PIM-CF showed a broad peak at 3460 cm^{-1} corresponding to the O–H vibration of a hydrogen-bonded water molecule in the inter-lamellar space of NiOOH/$Ni(OH)_2$ and ν-Ni–OH vibrations at ≤500 cm^{-1} (Figure 2C).[38,39] The XRD pattern with a slight hump at a 2θ value of 36° and increase in the area under the peak at 43° was attributed to the presence of Ni (111) and Ni (200) facets

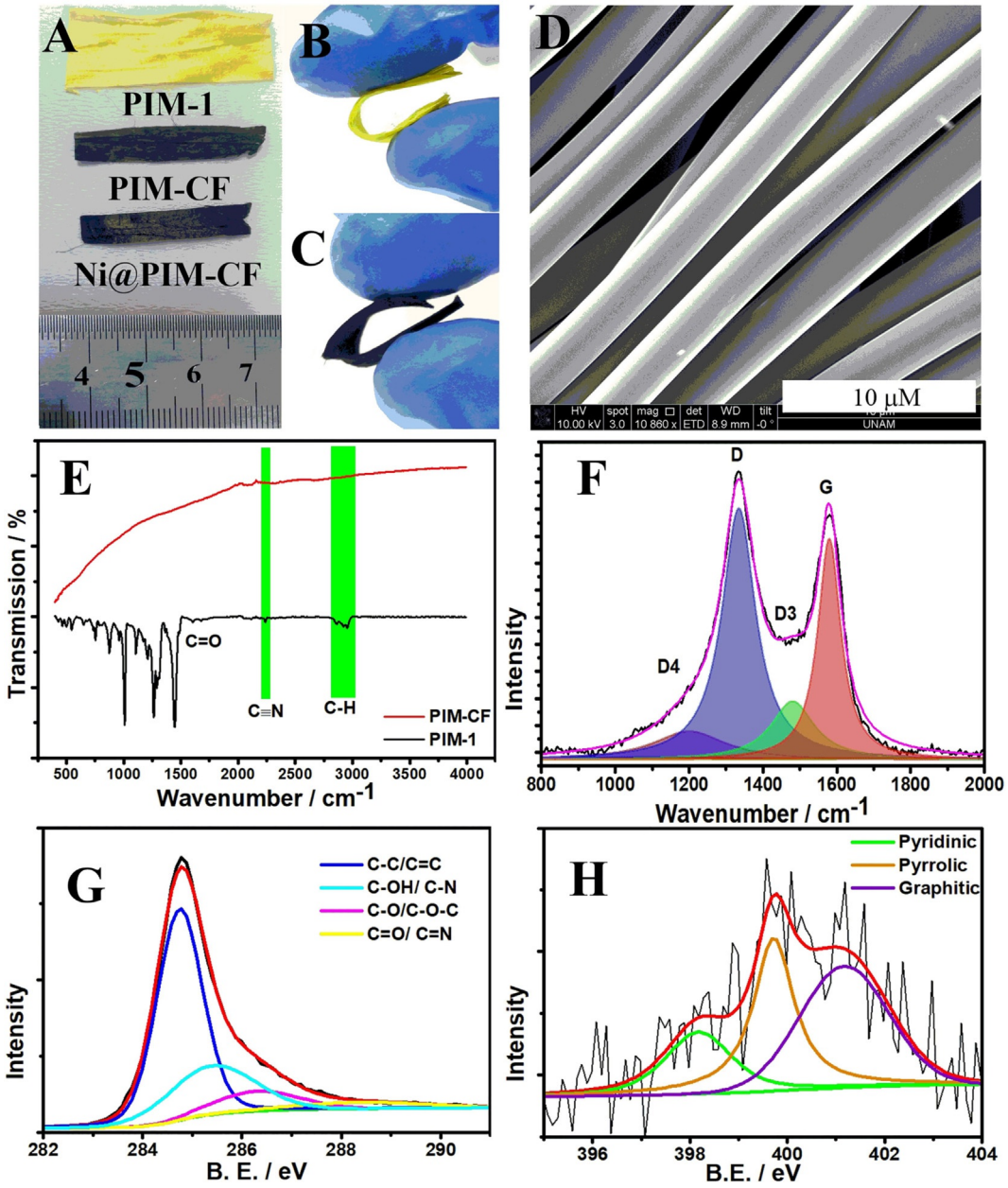

Figure 1. A) A representative photograph of PIM-1, PIM-CF, and Ni@PIM-CF. B) The free-standing flexible PIM-1 and C) Ni@PIM-CF. D) SEM image of PIM-CF (scale bar: 10 μM). E) FTIR spectra of PIM-1 and PIM-CF. F) Raman spectra of PIM-CF. High-resolution XPS spectrum of G) carbon and H) nitrogen in PIM-CF.

of $Ni(OH)_2$ (Figure S2 in the Supporting Information).[38] The I_D/I_G ratio of the Raman spectra changed from 1.66 to 1.48 after Ni deposition on Ni@PIM-CF, which showed an increase in graphitic carbon or a decrease in disordered carbon after $NiOOH/Ni(OH)_2$ deposition (Figure 2D). This was expected owing to a favorable reaction between the disordered carbon and O_3 rather than the graphitic carbon, which led to a faster decomposition of the disordered carbon during $NiOOH/Ni(OH)_2$ deposition. The increase in the intensity of the C=O/C=N peak in Ni@PIM-CF compared with that in PIM-CF was assigned to a functionalized carbon surface or to the change in the nitrogen doping position owing to O_3 exposure during ALD. The O_3 treatment can increase the amount of C=O.

The high-resolution XPS spectra further confirmed the state of the Ni on Ni@PIM-CF (Figure 2F). This Ni $2p_{3/2}$ spectrum did not contain the characteristic peaks for metallic Ni, that is, Ni^0 and NiO, at 852.6 and 854.5 eV, respectively. The absence of a low-binding energy feature at 530.1 eV, which was assigned to the lattice oxygen NiO, further ruled out the presence of NiO in Ni@PIM-CF (Figures S3B and S7B in the Supporting Information). Ni $2P_{3/2}$ had a maximum binding energy of approximately 856 eV, indicating presence of a $NiOOH/Ni(OH)_2$ mixture. This mixture had high binding energy signals at 531.4 eV (O 1s), which further confirmed the presence of oxyhydroxide species of Ni in Ni@PIM-CF. However, the oxygen XPS spectrum was expected to be a cumulative contribution from $NiOOH/Ni(OH)_2$

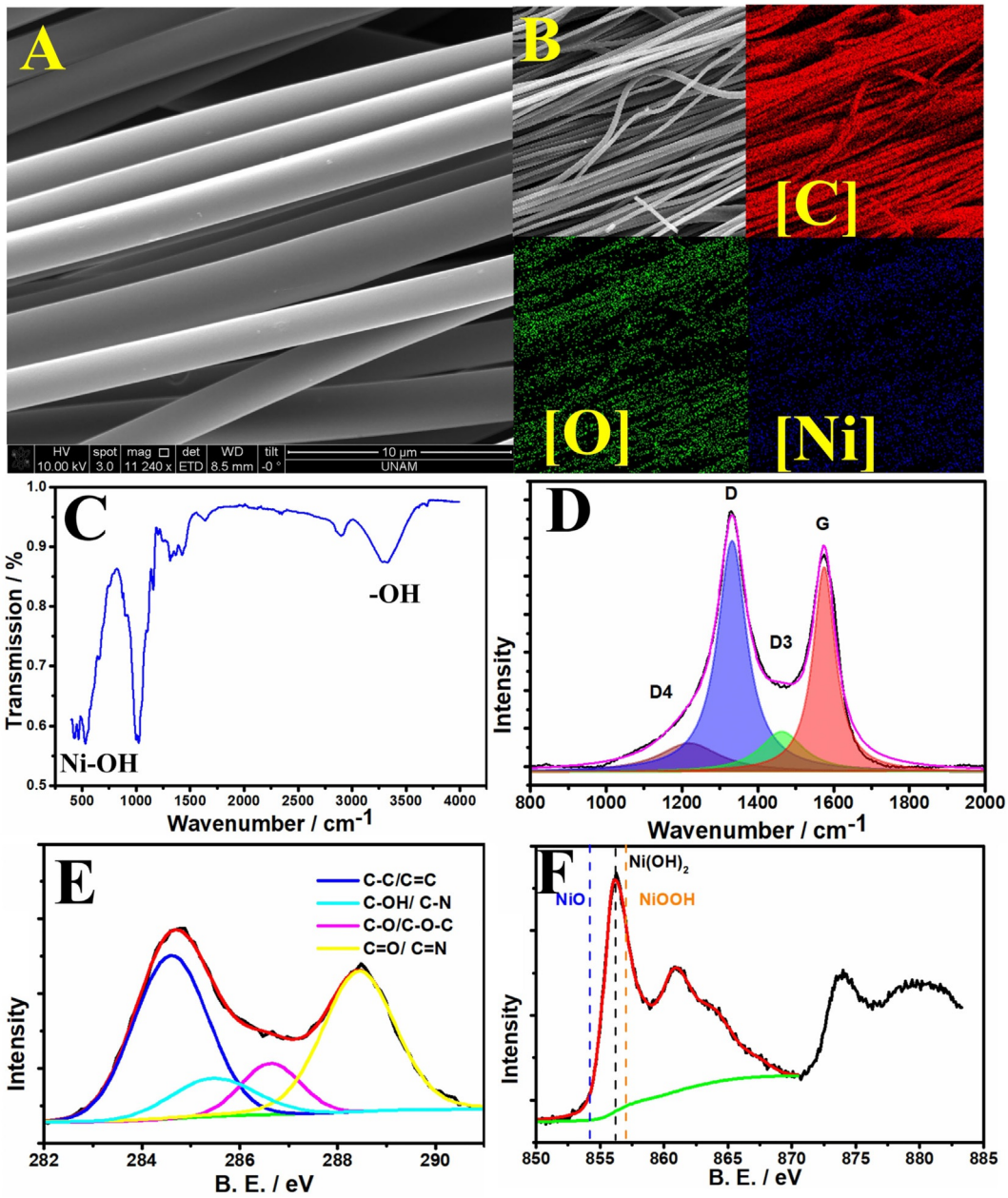

Figure 2. A) SEM image of Ni@PIM-CF (scale bar: 10 µM) with B) elemental mapping of carbon, oxygen, and nickel. C) FTIR, D) Raman, and high-resolution XPS spectra of E) carbon and F) nickel for Ni@PIM-CF.

and C–OH/C–O–C/C=O. Therefore, to confirm the oxyhydroxide state of Ni, the 3d state feature in the valance band was measured; the lack of an intense peak at 2.4 eV further proved the absence of NiO and the presence of the NiOOH/$Ni(OH)_2$ with an intense peak at approximately 3 eV as reported previously (Figures S3C and S7C in the Supporting Information).[40] Overall, the high-resolution spectra of Ni and O and the valance-band position validated that Ni was present in Ni@PIM-CF as a mixture of NiOOH/$Ni(OH)_2$.[40,41] The C1s spectra of PIM-CF and Ni@PIM-CF clearly showed that oxygenated carbon [285.5, 286.0, (288 ± 0.2) eV] increased after NiOOH/$Ni(OH)_2$ deposition owing to the reaction between O_3 and PIM-CF. Overall, the atomic O/C ratio increased from 0.054 to 0.82 after NiOOH/$Ni(OH)_2$ deposition.

According to inductively coupled plasma-mass spectrometry (ICP-MS), 0.95% Ni was loaded on Ni@PIM-CF. Thermogravimetric analysis (TGA, Figure S8 in the Supporting Information) of PIM-CF and Ni@PIM-CF confirmed the formation of some functional groups during Ni deposition that decomposed above 400 °C in Ni@PIM-CF. Therefore, it also proved the formation of partial amorphous carbon during Ni ALD, which was in line with the Raman spectra. The surface areas measured by N_2 adsorption isotherms by multipoint analysis according to the Brunauer–Emmet–Teller (BET) model for PIM-CF and

Ni@PIM-CF (Figure S9 in the Supporting Information) were 53 and 239 $m^2 g^{-1}$, respectively. Because the whole BET surface area is not electrocatalytically active, an electrochemically active surface area (ECSA) was estimated. The ECSA was estimated from the charge of the reduction of $Ni(OH)_2$ to Ni with the charge density of 514 $\mu C\,cm_{Ni}^{-2}$ for one monolayer of OH adsorption on the flat Ni surface (Figure S10 in the Supporting Information), which was 0.028 cm^{-2}.[42] The roughness factor (RF) was estimated by dividing ECSA by the geometric surface area, that is, 0.056.[1] Conventionally, it has been accepted that 10% efficient solar water-splitting devices should operate at 10 $mA\,cm^{-2}$, below approximately 0.45 V overpotential (η_{10}) for overall OER and HER.[2] Therefore, η_{10} values at 10 $mA\,cm^{-2}$ were analyzed and compared with those for Pt/C and Ru/C. The important analysis and results of HER and OER such as onset overpotential, potential to reach the current densities (j_g) at 10 $mA\,cm^{-2}$ based on the geometric area, turnover frequency (TOF), and mass activity were compared and are summarized in Table 1 (calculation details are elaborated in the Supporting Information).

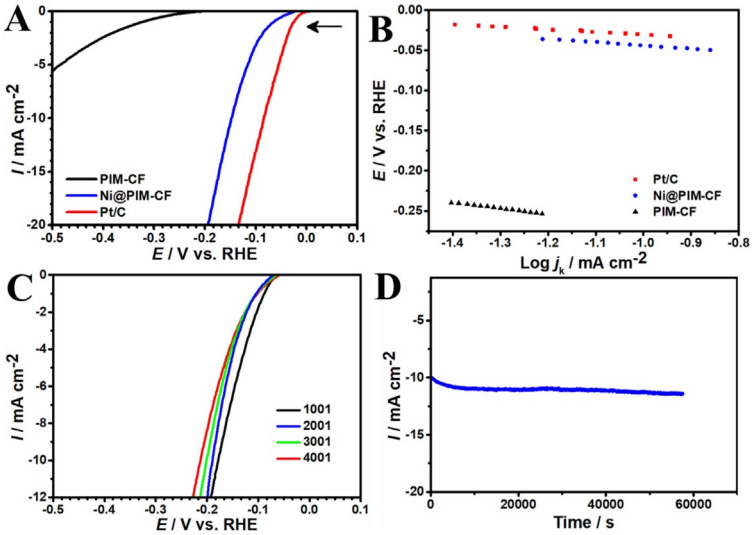

Figure 3. A) LSVs measured over PIM-CF and Ni@PIM-CF towards HER with a sweep rate of 1 $mV\,s^{-1}$ under N_2-saturated 0.1 M KOH and B) Tafel plots (data used from Figure 3 A). C) LSVs measured after 1000, 2000, 3000, and 4000 CVs (potential −0.2 to 1.0 V vs. RHE at 100 $mV\,s^{-1}$) with a sweep rate of 1 $mV\,s^{-1}$ and D) durability with CA (after CV measurements) over Ni@PIM-CF towards HER.

The hydrogen evolution was studied in 0.1 M KOH, and results were compared with the standard Pt/C catalyst, which is reported as the best HER catalyst so far.[43] The electrocatalytic activity of PIM-CF, Ni@PIM-CF, and Pt/C towards HER in 0.1 M KOH was screened through linear sweep voltammetry (LSV; Figure 3 A). The drastic anodic shift of approximately 190 mV in the onset potential of Ni@PIM-CF compared to PIM-CF noticeably disclosed an effect of $NiOOH/Ni(OH)_2$ catalyst deposition on PIM-CF. The onset potential of HER over Ni@PIM-CF was comparable with the Pt/C catalyst (Figure 3 A) and anodic with previously reported NiO, Ni nanomaterials[44] catalysts reported previously. The TOF value and exchange current density (i_0) obtained for Ni@PIM-CF and Pt/C were 0.029 s^{-1} and 0.82 $mA\,cm^{-2}$, and 0.035 s^{-1} and 0.86 $mA\,cm^{-2}$, respectively, which showed that the HER over Ni@PIM-CF produced almost an equivalent amount of hydrogen as over Pt/C. The portable and flexible energy devices must be lightweight with better HER efficiency. In this context, mass activity was measured to evaluate the efficient catalytic activity of Ni@PIM-CF and Pt/C towards HER. Ni@PIM-CF had a mass activity of 122.55 $A\,g^{-1}$ whereas that of Pt/C was 70.68 $A\,g^{-1}$; therefore, Ni@PIM-CF was a more efficient HER catalyst than Pt/C (20% PtC with <5 nm particle size) in terms of the mass activity.

HER is generally a process through the Volmer, Heyrovsky, and Tafel reactions [Eqs. (1)–(3)]. In addition, HER in alkaline media could be a process through two possible pathways, that is, Volmer–Heyrovsky or Volmer–Tafel pathways.[42,44]

$$H_2O + e^- \rightarrow H_{ad} + OH^- \quad \text{Volmer reaction} \quad (1)$$

$$H_2O + H_{ad} + e^- \rightarrow H_2 + OH^- \quad \text{Heyrovsky reaction} \quad (2)$$

$$H_{ad} + H_{ad} \rightarrow H_2 \quad \text{Tafel reaction} \quad (3)$$

In either pathway, the first process (Volmer) involves adsorption of a water molecule on the catalyst followed by splitting of H_2O into H_{ad} and OH^-. As postulated, Ni^{2+} or more unfilled d orbitals can electrostatically adsorb OH^- on $Ni(OH)_2$,[44,45] whereas nearby NiOOH or Ni^0 would facilitate H adsorption.[46] Therefore, the Volmer process involves synergistic HER activity of $NiOOH/Ni(OH)_2$ similar to NiO/Ni.[44] It further avoids surface poisoning by OH^- or H^+ adsorption in contrast to pure Ni or NiO catalysts.[44] Although an applied potential can reduce Ni^{III} into its low oxidation state of Ni^0, this process is not necessary completed, as reported in the literature.[47] The slopes of the Tafel plots obtained over Ni@PIM-CF were close to 40 and not 120 $mV\,dec^{-1}$, which further proved that the rate-limiting step

Table 1. Electrochemical results of different catalysts towards HER in 0.1 M KOH.

Catalyst	η[a] [mV]	η[b] [mV]	Tafel slope [$mV\,dec^{-1}$]	j_g[c] [$mA\,cm^{-2}$]	j_s [$mA\,cm^{-2}$]	TOF[c] [s^{-1}]	i_0 [$mA\,cm^{-2}$]	MA [$A\,g^{-1}$]
PIM-CF	−230	–	73	–	–	–	–	–
Ni@PIM-CF	−40	−147	41	10	0.42	0.029	0.82	122.5
Pt/C	−10	−81	32	22	0.64	0.035	0.86	70.68

[a] Onset potential. [b] η at 10 $mA\,cm^{-2}$. [c] at $\eta = -0.147$ V.

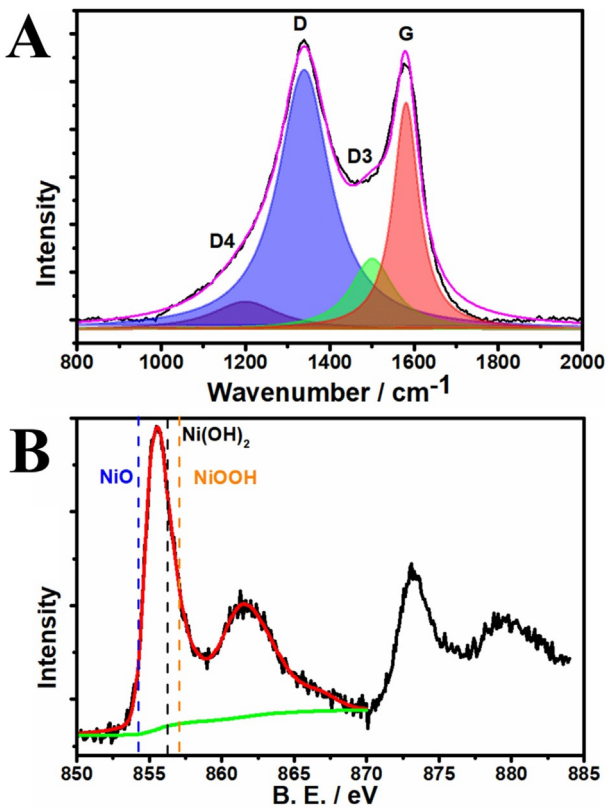

Figure 4. Post-catalysis analysis after HER durability studies by A) Raman spectroscopy and B) high-resolution Ni-XPS obtained for Ni@PIM-CF.

was not the Volmer reaction but the Heyrovsky reaction, whereas in the case of Pt/C, the Tafel slope was close to 30 mV dec^{-1}, indicating that the Tafel reaction was the rate-limiting step.[48] Therefore, we propose that the HER mechanism over Ni@PIM-CF favored the Volmer–Tafel pathway whereas Pt/C favored the Volmer–Heyrovsky pathway.

In addition to all these properties, the durability or stability of the catalyst is another important characteristic feature to evaluate the efficiency of the catalyst. Therefore, the stability of Ni@PIM-CF was analyzed by measuring 4000 CVs followed by continuous hydrogen production by chronoamperometry (the same electrode was used after CV measurements) at 12 mA cm^{-2} for 16 h (Figure 3C,D). The LSV measured after 4000 cycles showed a slight cathodic shift in the HER catalysis (Figure 3C) and almost constant hydrogen production for 16 h (Figure 3D). The structural and compositional stability of the Ni and carbon in Ni@PIM-CF after HER stability (CV and CA) were also studied through XPS and Raman spectroscopy (Figure 4A,B). A slight shift towards a lower binding energy was observed in the XPS spectrum of Ni, which was attributed to the partial reduction of Ni^{III} to Ni^{II} as an effect of the applied potentials during HER (Figures 2, 4B). The atomic percentage of Ni was altered from 8 to 3% in comparison with the pristine Ni@PIM-CF. The I_D/I_G ratio was 2.3 after HER measurements (Figure 4A). Therefore, partial removal of NiOOH/$Ni(OH)_2$ owing to the changes in the PIM-CF structure cannot be ruled out. Overall, comparable TOF values, i_o, and onset potential of Ni@PIM-CF with Pt/C and a higher mass activity and lower cost of Ni in comparison with Pt makes Ni@PIM-CF a better catalyst for use in water-splitting devices.

The sluggish kinetics and large overpotential (η_{OER}) required for OER demands new efficient and stable catalyst for the OER. The OER catalysis over Ni@PIM-CF was analyzed by LSV (Figure 5A). The cathodic shift in the onset potential obtained over Ni@PIM-CF as compared with PIM-CF unambiguously demonstrated the catalytic activity of NiOOH/$Ni(OH)_2$ towards OER (important parameters are summarized in Figure 6). The overpotential was estimated as $\eta_{OER} = E$ [vs. reversible hydrogen electrode (RHE)] − 1.23 V.[1] The TOF value measured at 390.5 mV was 0.029, which was approximately threefold[49–51] or 1.5-fold[52] higher than for IrO_2. Furthermore, η_{OER} at 10 mA cm^{-2} over Ni@PIM-CF was 390.5 mV, which was close to the η_{OER} at 10 mA cm^{-2} over RuO_2 (390 mV)[2] and Ni@NC (390 mV).[23] The OER mechanism over Ni@PIM-CF was a complex reaction, as described in Scheme 1.[12] The Tafel slope obtained over Ni@PIM-CF was approximately 50 mV dec^{-1}, which was close to 60 mV dec^{-1} (Figure 5B). Therefore, the rate-limiting step was expected to be the conversion of SOH to SO^-, as shown in the OER mechanism.[12]

The stability of Ni@PIM-CF towards OER was analyzed by CV measurements for 4000 cycles in the potential window of 0.7 to 1.7 V vs. RHE at a sweep rate of 100 mV s^{-1}. The LSVs measured after every 1000 cycles are shown in Figure 5C. The durability of the same electrode was further evaluated by continuous oxygen production with CA (Figure 5D). The Ni@PIM-CF electrode was characterized after OER to determine the states of Ni and carbon composition with high-resolution XPS and Raman spectroscopy (Figure 7). The XPS spectrum of Ni resem-

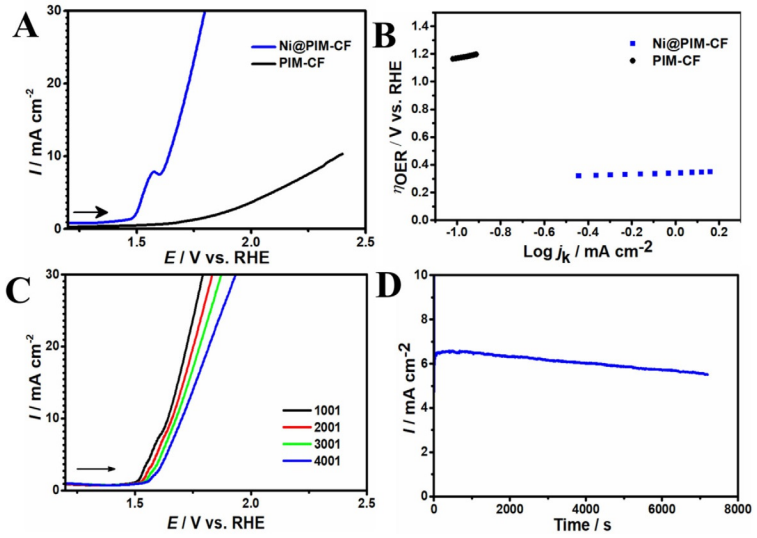

Figure 5. A) LSVs measured over PIM-CF and Ni@PIM-CF towards OER with a sweep rate of 1 mV s^{-1} in N_2-saturated 0.1 M KOH and B) Tafel plots (data used from Figure 5A). C) LSVs measured after 1000, 2000, 3000, and 4000 CVs (potential range 0.7 to 1.7 V vs. RHE at 100 mV s^{-1}) with a sweep rate of 1 mV s^{-1} and D) durability with CA (after CV stability measurements) over Ni@PIM-CF towards OER.

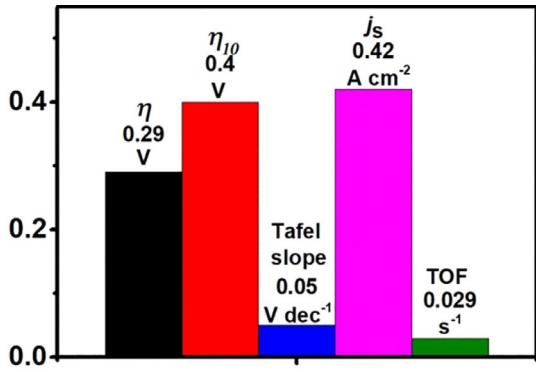

Figure 6. Summary of important OER properties (data used from Figure 5A, B).

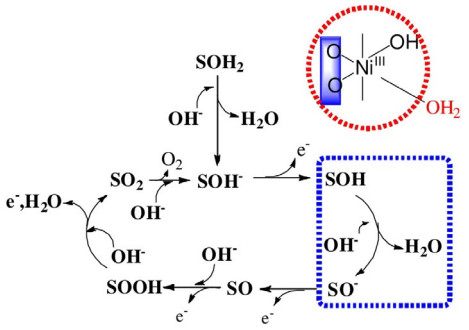

Scheme 1. OER mechanism over Ni@PIM-CF in which S = surfaquo group (red dotted circle) and the rate-limiting step is shown in a blue dotted square.[12]

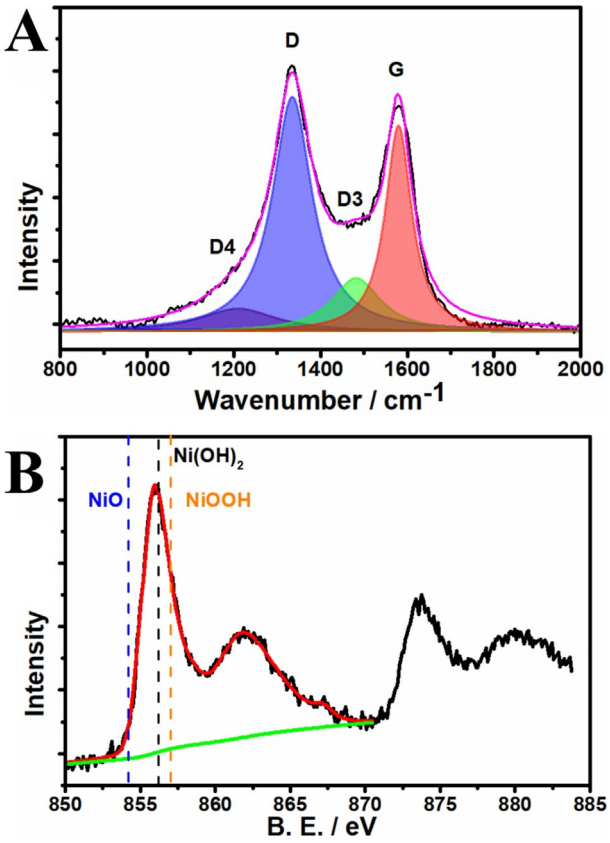

Figure 7. Post-catalysis analysis after OER durability studies by A) Raman spectroscopy and B) high-resolution Ni-XPS obtained for Ni@PIM-CF.

bled that of the pristine Ni@PIM-CF, which demonstrated that Ni remained in the oxyhydroxy state after OER, which was expected owing to the high positive applied potential. The atomic percentage of Ni after OER was slightly decreased by 0.85% compared to before, which was attributed to the partial breaking of the C–C bonds, which ultimately resulted in the removal of $NiOOH/Ni(OH)_2$ from the electrode surface. Raman spectroscopy was performed to evaluate stability of PIM-CF fibers before and after OER. The small increase in the I_D/I_G ratio from 1.66 to 1.7 inferred partial breaking of the C–C bonds. This supported the slight decrease in the Ni atomic percentage in the XPS analysis.

LSV measurements were also performed after bending followed by re-straightening of the electrodes (Figure S11 in the Supporting Information). Negligible differences were observed after bending followed by re-straightening of the electrodes, which further proved the flexibility of the electrode with comparable catalytic activity with regard to bending and non-bending position. Finally, PIM-CF fibers, owing to their aligned porous support, behaved like a bunch of 1D fibers that can easily diffuse gas and intermediate products to and from the electrode and solution. Furthermore, ALD-decorated $NiOOH/Ni(OH)_2$ on PIM-CF was highly stable, which might be owing to crucial association between nitrogen and Ni, as depicted earlier.[23] $NiOOH/Ni(OH)_2$ ALD-coated, free-standing, flexible, well aligned, binder-free, electrospun PIM-1 N-doped carbon fibers showed stable and high catalytic activity towards both HER and OER in alkaline media.

Conclusions

The electrospun polymers of intrinsic microporosity (PIM-1) fibers retained their flexibility after carbonization and even after atomic layer deposition (ALD) of $NiOOH/Ni(OH)_2$. Therefore, Ni@PIM-CF was achieved. The $NiOOH/Ni(OH)_2$ ALD-modified, 1D-aligned, N-doped, electrospun PIM-1 carbon nanofibers (PIM-CF) proved to be a highly efficient nanocatalyst towards hydrogen (HER) and oxygen evolution reaction (OER) in an alkaline medium. The low cost of Ni materials, abundant availability, almost equivalent catalytic activity with the benchmark catalysts, and stability makes this electrode material highly efficient. In addition, the free-standing, binder-free, and flexible properties of this electrode enhance its applicability in flexible energy devices. In summary, Ni@PIM-CF showed remarkable turnover frequencies ($0.029\ s^{-1}$) with small Tafel slopes of 41 and $50\ mV\,dec^{-1}$ for HER and OER, respectively, and small overpotential, which makes it a highly efficient and kinetically enhanced catalysts for HER and OER at the same pH value. A durability study under cyclic voltammetry and continuous H_2 and O_2 production with chronoamperometry clearly demonstrated its stability over a long duration (>16 h). The combination of nitrogen-doped PIM-CF with ALD of NiOOH/

$Ni(OH)_2$ renders Ni@PIM-CF as a promising flexible free-standing electrode with efficient catalysis and long-term stability for water splitting in an alkaline medium.

Experimental Section

Synthesis of electrospun PIM-1

The synthesis and characterization of PIM-1 powder as well as the electrospinning process were reported in our previous study.[35] PIM-1 powder was dissolved in 1,1,2,2-tetrachloroethane to make a solution with a 23 wt% concentration. This solution was heated at 60 °C for 1 h with stirring at 500 rpm. It was stirred at room temperature overnight and degassed prior to electrospinning. The electrospinning was performed with a 3 mL syringe equipped with a blunt metal needle with a 0.5 mm inner diameter, a syringe pump (KD scientific, KDS 101), and an aluminum-foil-wrapped metal plate. 2 mL of PIM-1 solution was pumped at a rate of 0.5 mL h^{-1} with an applied potential of 11–12 kV and a distance between the needle and metal plate of 18 cm. The fibers were separated from the aluminum foil with the help of methanol and dried in an oven at 130 °C under vacuum for 24 h to remove the solvent residues.

Pyrolysis of electrospun PIM-1

As-prepared electrospun PIM-1 nanofibers were pyrolyzed in a tubular furnace at 800 °C with a heating rate of 5 °C min^{-1} for 3 h under an Ar flow (100 sccm). The sample was allowed to cool and used further for $NiOOH/Ni(OH)_2$ deposition.

ALD of $NiOOH/Ni(OH)_2$ on PIM-CF (Ni@PIM-CF)

The $NiOOH/Ni(OH)_2$ was deposited on PIM-CF by using a Savannah S100 ALD reactor (Ultratech Inc.). The sample was loaded in the ALD reaction chamber and heated at 140 °C. The bis(cyclopentadienyl)nickel(II) precursor was preheated to 80 °C, and O_3 was used as a counter reactant. A Cambridge NanoTech Savannah Ozone generator was used to produce O_3 from pure O_2. Dynamic vacuum conditions were used for the uniform coating of $NiOOH/Ni(OH)_2$ on PIM-CF. The pulse, exposure, and purge times for the bis(cyclopentadienyl)nickel(II) precursor were 1, 10, and 10 s, respectively, and for O_3 1, 10, and 5 s, respectively. Prior to $NiOOH/Ni(OH)_2$ deposition, PIM-CF were first treated with O_3 (with the same conditions for one ALD cycle) to produce –OH functional groups on the surface. 100 cycles of ALD were deposited to acquire Ni@PIM-CF.[53] The schematic representation of the experimental procedure is illustrated in Scheme 2.

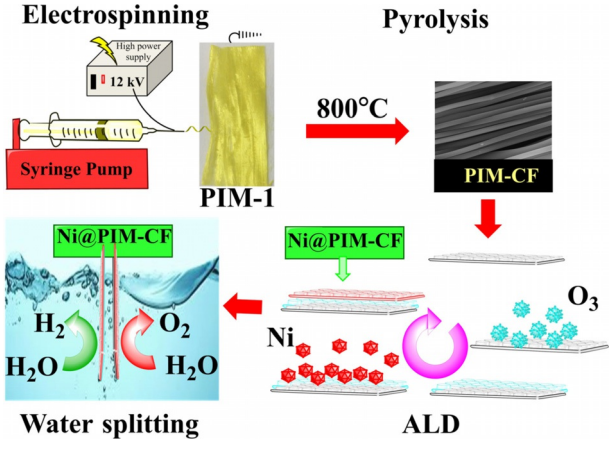

Scheme 2. Fabrication of Ni@PIM-CF and its catalysis of the water splitting reaction.

Conflict of interest

The authors declare no conflict of interest.

Keywords: atomic layer deposition · carbon fibers · electrospinning · nickel · water splitting

[1] M. F. Tovini, B. Patil, C. Koz, T. Uyar, E. Yilmaz, *Nanotechnology* **2018**, *29*, 475401.
[2] C. C. L. McCrory, S. Jung, I. M. Ferrer, S. M. Chatman, J. C. Peters, T. F. Jaramillo, *J. Am. Chem. Soc.* **2015**, *137*, 4347–4357.
[3] T. G. Ulusoy Ghobadi, B. Patil, F. Karadas, A. K. Okyay, E. Yilmaz, *ACS Omega* **2017**, *2*, 8319–8329.
[4] S. Cobo, J. Heidkamp, P. A. Jacques, J. Fize, V. Fourmond, L. Guetaz, B. Jousselme, V. Ivanova, H. Dau, S. Palacin, M. Fontecave, V. Artero, *Nat. Mater.* **2012**, *11*, 802–807.
[5] L. Liao, Q. Zhang, Z. Su, Z. Zhao, Y. Wang, Y. Li, X. Lu, D. Wei, G. Feng, Q. Yu, X. Cai, J. Zhao, Z. Ren, H. Fang, F. Robles-Hernandez, S. Baldelli, J. Bao, *Nat. Nanotechnol.* **2014**, *9*, 69–73.
[6] J.-W. Jang, C. Du, Y. Ye, Y. Lin, X. Yao, J. Thorne, E. Liu, G. McMahon, J. Zhu, A. Javey, J. Guo, D. Wang, *Nat. Commun.* **2015**, *6*, 7447.
[7] W. Sheng, M. Myint, J. G. Chen, Y. Yan, *Energy Environ. Sci.* **2013**, *6*, 1509–1512.
[8] J. Greeley, T. F. Jaramillo, J. Bonde, I. Chorkendorff, J. K. Nørskov, *Nat. Mater.* **2006**, *5*, 909–913.
[9] B. Chang, G. Zhao, Y. Shao, L. Zhang, B. Huang, Y. Wu, X. Hao, *J. Mater. Chem. A* **2017**, *5*, 18038–18043.
[10] B. Chang, J. Yang, Y. Shao, L. Zhang, W. Fan, B. Huang, Y. Wu, X. Hao, *ChemSusChem* **2018**, *11*, 3198–3207.
[11] Y. Zhong, B. Chang, Y. Shao, C. Xu, Y. Wu, X. Hao, *ChemSusChem* **2019**, https://doi.org/10.1002/cssc.201802091.
[12] M. E. G. Lyons, R. L. Doyle, I. Godwin, M. O'Brien, L. Russell, *J. Electrochem. Soc.* **2012**, *159*, H932–H944.
[13] Y. Fan, Y. Wu, G. Clavel, M. H. Raza, P. Amsalem, N. Koch, N. Pinna, *ACS Appl. Energy Mater.* **2018**, *1*, 4554–4563.
[14] Z. M. Huang, Y. Z. Zhang, M. Kotaki, S. Ramakrishna, *Compos. Sci. Technol.* **2003**, *63*, 2223–2253.
[15] F. Kayaci, S. Vempati, C. Ozgit-Akgun, I. Donmez, N. Biyikli, T. Uyar, *Nanoscale* **2014**, *6*, 5735.
[16] F. Kayaci, C. Ozgit-Akgun, I. Donmez, N. Biyikli, T. Uyar, *ACS Appl. Mater. Interfaces* **2012**, *4*, 6185–6194.
[17] J. S. Bonso, G. D. Kalaw, J. P. Ferraris, *J. Mater. Chem. A* **2014**, *2*, 418–424.
[18] A. Senthamizhan, A. Celebioglu, B. Balusamy, T. Uyar, *Sci. Rep.* **2015**, *5*, 15608.
[19] A. Senthamizhan, A. Celebioglu, S. Bayir, M. Gorur, E. Doganci, F. Yilmaz, T. Uyar, *ACS Appl. Mater. Interfaces* **2015**, *7*, 21038–21046.
[20] H. J. Kim, D. G. Kim, K. Lee, Y. Baek, Y. Yoo, Y. S. Kim, B. G. Kim, J. C. Lee, *Sci. Rep.* **2016**, *6*, 36078.
[21] B. Satilmis, T. Uyar, *Appl. Surf. Sci.* **2018**, *453*, 220–229.
[22] P. M. Budd, B. S. Ghanem, S. Makhseed, N. B. McKeown, K. J. Msayib, C. E. Tattershall, *Chem. Commun.* **2004**, 230–231.
[23] J. Ren, M. Antonietti, T. P. Fellinger, *Adv. Energy Mater.* **2015**, *5*, 1401660.
[24] M. A. Khalily, M. Yurderi, A. Haider, A. Bulut, B. Patil, M. Zahmakiran, T. Uyar, *ACS Appl. Mater. Interfaces* **2018**, *10*, 26162–26169.
[25] L. Shen, Q. Che, H. Li, X. Zhang, *Adv. Funct. Mater.* **2014**, *24*, 2630–2637.
[26] B. Qu, X. Yu, Y. Chen, C. Zhu, C. Li, Z. Yin, X. Zhang, *ACS Appl. Mater. Interfaces* **2015**, *7*, 14170–14175.
[27] M. Leskelä, M. Ritala, *Angew. Chem. Int. Ed.* **2003**, *42*, 5548–5554; *Angew. Chem.* **2003**, *115*, 5706–5713.
[28] M. Knez, K. Nielsch, L. Niinistö, *Adv. Mater.* **2007**, *19*, 3425–3438.

[29] S. M. George, *Chem. Rev.* **2010**, *110*, 111.
[30] H. Van Bui, F. Grillo, J. R. Van Ommen, *Chem. Commun.* **2017**, *53*, 45 – 71.
[31] A. Celebioglu, K. S. Ranjith, H. Eren, N. Biyikli, T. Uyar, *Sci. Rep.* **2017**, *7*, 13401.
[32] O. Arslan, F. Topuz, H. Eren, N. Biyikli, T. Uyar, *New J. Chem.* **2017**, *41*, 4145 – 4156.
[33] F. Kayaci, S. Vempati, I. Donmez, N. Biyikli, T. Uyar, *Nanoscale* **2014**, *6*, 10224 – 10234.
[34] K. S. Ranjith, A. Celebioglu, H. Eren, N. Biyikli, T. Uyar, *Adv. Mater. Interfaces* **2017**, *4*, 1700640.
[35] B. Satilmis, T. Uyar, *J. Colloid Interface Sci.* **2018**, *516*, 317 – 324.
[36] B. Satilmis, P. M. Budd, *RSC Adv.* **2014**, *4*, 52189 – 52198.
[37] O. Salinas, X. Ma, E. Litwiller, I. Pinnau, *J. Membr. Sci.* **2016**, *504*, 133 – 140.
[38] L. Xu, Y. S. Ding, C. H. Chen, L. Zhao, C. Rimkus, R. Joesten, S. L. Suib, *Chem. Mater.* **2008**, *20*, 308 – 316.
[39] Z. Yan, H. Sun, X. Chen, H. Liu, Y. Zhao, H. Li, W. Xie, F. Cheng, J. Chen, *Nat. Commun.* **2018**, *9*, 2373.
[40] N. Weidler, J. Schuch, F. Knaus, P. Stenner, S. Hoch, A. Maljusch, R. Schäfer, B. Kaiser, W. Jaegermann, *J. Phys. Chem. C* **2017**, *121*, 6455 – 6463.
[41] A. P. Grosvenor, M. C. Biesinger, R. S. C. Smart, N. S. McIntyre, *Surf. Sci.* **2006**, *600*, 1771 – 1779.
[42] Z. Zhuang, S. A. Giles, J. Zheng, G. R. Jenness, S. Caratzoulas, D. G. Vlachos, Y. Yan, *Nat. Commun.* **2016**, *7*, 10141.
[43] B. E. Conway, B. V. Tilak, *Electrochim. Acta* **2002**, *47*, 3571 – 3594.
[44] M. Gong, W. Zhou, M. C. Tsai, J. Zhou, M. Guan, M. C. Lin, B. Zhang, Y. Hu, D. Y. Wang, J. Yang, S. J. Pennycook, B. J. Hwang, H. Dai, *Nat. Commun.* **2014**, *5*, 4695.
[45] P. Sirisinudomkit, P. Iamprasertkun, A. Krittayavathananon, T. Pettong, P. Dittanet, M. Sawangphruk, *Sci. Rep.* **2017**, *7*, 1124.
[46] Z. Mao, R. E. White, *J. Electrochem. Soc.* **1992**, *139*, 1282 – 1289.
[47] D. S. Hall, C. Bock, B. R. MacDougall, *J. Electrochem. Soc.* **2013**, *160*, F235 – F243.
[48] M. Qin, W. A. Maza, B. M. Stratakes, S. R. Ahrenholtz, A. J. Morris, Z. He, *J. Electrochem. Soc.* **2016**, *163*, F437 – F442.
[49] M. A. Khalily, B. Patil, E. Yilmaz, T. Uyar, *Nanoscale Adv.* **2019**, https://doi.org/10.1039/C8NA00330K.
[50] L. Trotochaud, J. K. Ranney, K. N. Williams, S. W. Boettcher, *J. Am. Chem. Soc.* **2012**, *134*, 17253 – 17261.
[51] A. T. Swesi, J. Masud, M. Nath, *Energy Environ. Sci.* **2016**, *9*, 1771 – 1782.
[52] G. Li, S. Li, J. Ge, C. Liu, W. Xing, *J. Mater. Chem. A* **2017**, *5*, 17221 – 17229.
[53] X. Tong, Y. Qin, X. Guo, O. Moutanabbir, X. Ao, E. Pippel, L. Zhang, M. Knez, *Small* **2012**, *8*, 3390 – 3395.

Manuscript received: October 30, 2018
Revised manuscript received: January 4, 2019
Accepted manuscript online: January 13, 2019
Version of record online: March 6, 2019